Single Atom Vibrational Spectroscopy in the Scanning Transmission Electron Microscope

F. S. Hage[1], G. Radtke[2*], D. M. Kepaptsoglou[1,3], M. Lazzeri[2], Q. M. Ramasse[1,4*]

[1]SuperSTEM Laboratory, SciTech Daresbury Campus, Daresbury WA4 4AD, United Kingdom

[2]Sorbonne Université, Muséum National d'Histoire Naturelle, UMR CNRS 7590, Institut de Minéralogie, de Physique des Matériaux et de Cosmochimie, 75005 Paris, France

[3]York NanoCentre & Department of Physics, University of York, Heslington, York YO10 5DD, United Kingdom

[4]School of Chemical and Process Engineering & School of Physics and Astronomy, University of Leeds, Leeds LS2 9JT, United Kingdom

*Correspondence to: qmramasse@superstem.org, guillaume.radtke@sorbonne-universite.fr

Abstract

Single-atom impurities and other atomic-scale defects can significantly alter the local vibrational response of solids and ultimately their macroscopic properties. Using high-resolution electron energy-loss spectroscopy in the electron microscope, we show that a single substitutional Si impurity in graphene induces a characteristic, localized modification of the vibrational response. Extensive ab initio calculations reveal the measured spectroscopic signature arises from defect-induced pseudo-localized phonon modes, i.e. resonant states resulting from the hybridization of the defect modes and the bulk continuum, whose energies can be directly matched to the experiments. This realizes the promise of vibrational spectroscopy in the electron microscope with single atom sensitivity, offering wide-reaching implications across the fields of physics, chemistry and materials science.

One Sentence Summary. We measure the localized vibrational signature of a single Si atom impurity in graphene in the electron microscope.

Main Text

Changes in the normal mode frequencies of dynamical systems arising from the presence of impurities have been studied as far back as the 19th century, resulting in the set of classical theorems now referred to as the Rayleigh Theorems (*1*, *2*). However, the modern theory of defect modes in crystals was established in the 1940s with the pioneering work of Lifschitz (*3*). A wealth of studies followed, mainly based on optical spectroscopies (*4*), which identified two types of non-trivial defect-induced modes known as localized and resonant modes. Resonant modes are also called quasi- or pseudo-localized modes because, despite being spatially extended, they involve a large amplitude vibration of the impurity itself. In turn, defect modes can control materials' properties such as electric and heat transport or more generally processes that are affected by the scattering of electrons or phonons. This can be exploited for instance to suppress heat propagation in thermoelectrics using rattler modes (*5*), to tune the superconductivity in 2-dimensional films (*6*) or the optoelectronic properties of conducting polymers (*7*). Although the existence of an atomically localized spectroscopic signature of single-atom defects has long been discussed (*8*) conventional vibrational spectroscopies typically average information over much larger lengthscales.

Vibrational electron energy loss spectroscopy (EELS) in the scanning transmission electron microscope (STEM) has recently emerged as a powerful means of probing the vibrational response of materials at a spatial resolution superior to other experimental techniques (*9*, *10*). Tip-enhanced Raman spectroscopy (TERS) (*11*) or inelastic electron tunneling spectroscopy (IETS) (*12*, *13*) provide high spatial and energy resolution alternatives, but they are strictly limited to surface experiments and therefore present challenges for a range of applications. Vibrational STEM-EELS on the other hand takes advantage of versatile probe-forming optics to offer ground-breaking capabilities: nanometer-scale thermometry (*14*), mapping of bulk and surface-phonon-polariton modes (*15*), establishing phonon dispersion diagrams from nano-objects (*16*), site-specific isotopic labeling in molecular aggregates (*17*). These reports highlight the complementarity of STEM-EELS with conventional vibrational spectroscopies whose energy resolution remains unmatched. However, the ultimate promise of vibrational STEM-EELS is to reach the single atom or molecular level, in the same way that modern microscopes enabled electronic structure analysis (*18*), plasmonic (*19*) and UV-optical response fingerprinting (*20*), or energy-dispersive X-ray spectroscopy (*21*) from single atoms. Atomically resolved phonon maps of bulk systems are preliminary steps in this direction (*22*).

Here, we use STEM-EELS to measure the localized vibrational signature of a single trivalent substitutional Si atom in single-layer graphene (Si@Gr). From ab initio simulations we attribute the measured atomic-scale spectroscopic response to scattering by pseudo-localized vibrational modes arising from a resonance between the Si impurity-specific modes and the bulk continuum.

Figure 1A illustrates how electron beam deflectors are adjusted to displace the EEL spectrometer entrance aperture by 69 mrad (or a 8.67 Å^{-1} momentum transfer) with respect to the bright field (BF) disc, so that these no longer overlap. Further details of the experimental geometry are

provided in the Supplementary Materials (SM), fig. S1. Compared to a conventional on-axis geometry where the EELS aperture is centered on the BF disc, this off-axis or dark-field EELS geometry significantly suppresses the relative contributions of electrons having undergone elastic delocalized phonon scattering, favoring instead highly localized impact phonon scattering (*23*). This approach makes it possible to record atomic resolution phonon scattering maps of nm-thick flakes of hexagonal boron nitride (*22*) or of single-layer graphene (fig. S2 in the SM), where the off-axis geometry is key since the on-axis EELS phonon response of graphene is vanishingly small (*24*). Note that the large beam convergence necessary for an atomic-size probe results in spectral integration over a range of momentum transfer in the sample plane. To achieve a signal-to-noise ratio sufficient for resolving the phonon loss spectrum fine structure, the electron beam is scanned repeatedly over a small window tightly defined around the impurity of interest while the spectrum intensity is accumulated (*25*).

Figure 1B shows a dark-field EEL spectrum from a single Si atom impurity in graphene ("Si", red) alongside that acquired from a comparably sized region of pristine graphene ("C", blue), located a mere few atoms away from the Si impurity. The relative positions of the two scanned regions are indicated by red (Si) and blue (C) boxes on the high-angle annular-dark-field (HAADF) image in fig. 1C. A close-up of the probed Si atom (fig. 1D) and the corresponding fine structure of the Si $L_{2,3}$ ionization edge (fig. S3C) confirm that the brighter contrast Si atom is trivalently substituted into the graphene lattice. Asymmetric annular-dark-field movies (aADF, thus denoted due to the off-axis geometry) were recorded during spectrum acquisition to monitor possible beam-induced structure modifications, while ensuring the probed atom remained centered within the scanned region. Averaged aADF movies are shown as insets in fig. 1B, with individual frames shown in the SM.

The Si and C spectra in fig. 1B are normalized to the maximum of their respective zero-loss peaks (ZLPs). As a result the tails of the ZLPs closely overlap immediately before the first observable loss features, allowing for a straightforward visual comparison of relative changes in energy loss due to inelastic scattering by phonons. Any change in spectrum intensity above the coinciding ZLP tails should be representative of differences in relative phonon scattering probability. The fine structure in the phonon energy range of the two recorded spectra is strikingly different. While the C spectrum is consistent with that of non-doped bulk graphene (*24*), the Si spectrum comprises phonon loss features at different energies.

Figure 1E shows in greater detail the phonon loss region of the spectra. The C spectrum exhibits two distinct loss peaks at 85 meV (685 cm^{-1}) and 170 meV (1371 cm^{-1}). Following Ref. (*24*), we assign these peaks to scattering by transverse (T) and longitudinal (L), acoustic (A) or optical (O) modes in graphene, respectively (the graphene phonon dispersion diagram is presented for reference in fig. S10). Spectral contributions of out-of-plane phonon modes are expected to be negligible as the incident electron beam is normal to the graphene plane. In spite of stemming from a position only a few atoms away, the Si spectrum shows a remarkably different phonon fine structure comprising a prominent loss peak at about 50 meV (403 cm^{-1}) and weaker

structures at 125 and 150 meV (1008 and 1209 cm^{-1}). To enhance the differences between the spectra, we subtracted the C from the Si spectrum: the "difference spectrum" is shown in fig. 1E-F. This process has the additional benefit of effectively subtracting the elastic scattering ZLP tail (making the reasonable assumption that the tail contribution, before any expected loss contribution, is similar between spectra) without possible errors associated with common background removal techniques, as discussed in the SM (fig. S4). The difference can thus be interpreted as a relative change in phonon scattering probability induced by the presence of the single Si atom impurity. Virtually identical results (in SM) were obtained from complementary measurements carried out in a different area of the sample. These experimental results lead to the remarkable conclusion that the single Si atom impurity in graphene possesses a characteristic vibrational signature localized at the atomic scale.

To gain insights into the physics associated with these results, we have calculated within the framework of density functional theory (DFT) (*26*) the vibrational spectrum of a large 96×96 supercell of graphene containing one substitutional Si atom, using periodic boundary conditions. The structure of the defect and computational details are presented in the SM. As discussed therein, the important features observed in the vibrational EEL spectra of graphene can safely be interpreted in terms of the phonon density of states (DOS) of the bulk. The local behavior of the DOS can be quantified by the projected phonon DOS (PPDOS) defined as $n^\kappa(\omega) = \sum_\nu |\mathbf{e}_\nu^\kappa|^2 \delta(\omega - \omega_\nu)$, where κ denotes a specific atom, ω_ν and $\mathbf{e}_\nu$ are the phonon angular frequency and normalized polarization, and the sum is carried over all the phonon modes ν of the supercell. Since in our experiments the momentum transfer occurs predominantly in the plane perpendicular to the electron beam trajectory, only the components of the phonon polarization parallel to the graphene plane are relevant. A tentative comparison to the experimental difference spectrum is then provided by combining the PPDOS projected on the Si atom n^{Si}, on its three carbon neighbors n^{C1}, and the bulk phonon DOS per atom n^{bulk}: $\tilde{n}(\omega) = [n^{\mathrm{Si}}(\omega) + 3n^{\mathrm{C1}}(\omega) - 4\,n^{\mathrm{bulk}}(\omega)]/4$. This differential PPDOS reflects the experimental spectrum averaging over the scanning window, which is expected to include contributions from the impurity's neighboring C atoms. The resulting differential PPDOS is shown in fig. 1F, after broadening to match the experimental resolution: it predicts all the main features of the experimental difference spectrum, including: a single peak at 50 meV (403 cm^{-1}), two overlapping peaks at 125 meV (1008 cm^{-1}) and 150 meV (1209 cm^{-1}), and "dips" centered around 100 meV (807 cm^{-1}) and 180 meV (1452 cm^{-1}).

The physical origin of these spectral features can be understood by considering the individual in-plane PPDOS employed to construct the differential PPDOS $\tilde{n}$ and those of carbon atoms at increasing distances away from the Si impurity: fig. 2A. The Si PPDOS is dominated by an intense peak at 50 meV, matching closely the low-energy experimental feature seen in fig. 1E. This peak is followed by a broad band with weaker structures at 105, 127 and 155 meV (847, 1024 and 1250 cm^{-1}).

The absence of intense features in the bulk graphene DOS at 50 meV implies that the corresponding modes should possess a degree of localization. Indeed, by inspecting the PPDOS of neighboring carbon atoms in fig. 2, it is evident that whereas the first two carbon neighbor shells coordinating the impurity still display traces of the 50 meV peak, its contribution is weak and the PPDOS of subsequent neighbors rapidly tend to the bulk signature, which is fully retrieved after 6 shells. Corresponding atomically resolved experimental spectra in fig. 2C, from a full spectrum image over equivalent carbon neighbor positions (fig. S8), exhibit an identical trend: the EELS signal reproduces the main features observed in the *in-plane* PPDOS.

It is instructive to consider a calculation performed on a smaller 13-atom fragment of C_{3v} symmetry centered on the impurity (fig. S9), decoupled from the supercell by artificially setting the interatomic force constants linking the fragment to the rest of the 96×96 supercell to zero. The fragment displays two modes with E symmetry at 52 and 124 meV (419 and 1000 cm^{-1}) involving large in-plane displacements of the Si, in-phase (mode A) or out-of-phase (mode B) with the neighboring carbon atoms: fig. 3. The resonances in the full Si@Gr system, simulated by the 96×96 supercell, can thus be interpreted as a hybridization of these local impurity modes with the vibrational continuum of the graphene bulk.

The associated atomic displacements, including those arising from the in-plane vibration of the silicon atom, do not decay far from the defect: the full system presents a delocalized continuum, a concept quantified with the inverse participation ratio analysis shown in the SM. However, these delocalized phonons modes possess an enhanced component atomically localized on the impurity: the power of EELS is the technique's ability to probe this quasi-localization thus revealing the paradoxical nature of defect-induced resonant modes. It is also remarkable that the experimentally measured ~25 meV (202 cm^{-1}) full-width at half-maximum (FWHM) of the impurity peak at 50 meV (fig. 1F) matches closely the intrinsic theory-predicted width of the quasi-resonant mode: fig. 3A. The experimental energy resolution is therefore not limiting and the EEL spectra capture faithfully the fine structure of the Si@Gr system's vibrational response.

Localized and resonant modes arising from point defects have been widely discussed (*8*). The former are characterized by frequencies lying out of the continuum of the unperturbed crystal and atomic amplitudes dying off faster-than-exponentially with increasing distance from the defect (*27*). By contrast, the latter occur at frequencies lying within the allowed bands of the host. The peculiar characteristics of these modes, where the vibrational amplitude does not vanish far from the defect but instead extends over the entire crystal, delayed their recognition (*28*). Furthermore, experimental observations of these effects have thus far been limited to indirect fingerprints, often at the macroscopic scale. Volgmann *et al.* (*13*) used SPM-IETS to detect a local energy-dependent increase in phonon DOS on a Ag (111) surface, which they attributed to a substitutional Cu atom. But the surface nature of these experiments and the lack of more direct visualization means precluded an unambiguous interpretation.

In contrast, the ability demonstrated here to measure directly at the atomic scale the localized component of the vibrational signature of a single impurity atom within a solid and to match the

observed spectral fine structure to theoretically predicted modes truly realizes the potential of phonon spectroscopy in the STEM. Single-atom defect sensitivity combined with isotope selectivity (*17*) and the ability to operate at cryogenic temperatures (*29*) marks STEM-EELS as a potentially unique technique for molecular chemistry, enabling experiments where a single functionalizing isotope is fingerprinted at the atomic scale through its vibrational signature. The approach should be applicable to three-dimensional structures, although challenges will arise from the complexity of the computational work necessary to inform these experiments. Nevertheless, the path to further tantalizing applications in solid state science opens up whereby the electron beam of the STEM is used both to assemble functional devices atom by atom (*30*) and to probe spectroscopically the resulting lattice dynamics and their coupling with other quasi-particles.

References and Notes

1. W. R. Hamilton, *Philos. Trans. R. Soc. London*. **124**, 247–308 (1834).

2. J. W. Strutt, *The Theory of Sound* (Cambridge University Press, Cambridge, 1887), vol. 1 of *Cambridge Library Collection - Physical Sciences*.

3. I. M. Lifšic, *Nuovo Cim.* **3**, 716–734 (1956).

4. A. S. Barker, A. J. Sievers, *Rev. Mod. Phys.* **47**, S1–S179 (1975).

5. D. J. Voneshen et al., *Nat. Mater.* **12**, 1028 (2013).

6. C. Brun et al., *Nat. Phys.* **10**, 444–450 (2014).

7. M. Shao et al., *Nat. Commun.* **5**, 3180 (2014).

8. R. F. Wallis, Ed., *Localized Excitations in Solids* (Springer US, Boston, MA, 1968; http://link.springer.com/10.1007/978-1-4899-6445-8).

9. O. L. Krivanek et al., *Nature*. **514**, 209 (2014).

10. T. Miyata et al., *Microscopy*. **63**, 377 (2014).

11. P. Z. El-Khoury et al., *Adv. Phys. X.* **1**, 35–54 (2016).

12. H. Gawronski, M. Mehlhorn, K. Morgenstern, *Science (80-.).* **319**, 930–933 (2008).

13. K. Volgmann et al., *Nat. Commun.* **5**, 1–6 (2014).

14. J. C. Idrobo et al., *Phys. Rev. Lett.* **120**, 95901 (2018).

15. M. J. Lagos, A. Trügler, U. Hohenester, P. E. Batson, *Nature*. **543**, 529–532 (2017).

16. F. S. Hage et al., *Sci. Adv.* **4**, eaar7495 (2018).

17. J. A. Hachtel et al., *Science (80-.).* **363**, 525–528 (2019).

18. K. Suenaga, M. Koshino, *Nature*. **468**, 1088–1090 (2010).

19. W. Zhou et al., *Nat. Nano.* **7**, 161–165 (2012).

20. F. S. Hage et al., *ACS Nano*. **12**, 1837–1848 (2018).

21. T. C. Lovejoy et al., *Appl. Phys. Lett.* **100**, 154101 (2012).

22. F. S. Hage, D. M. Kepaptsoglou, Q. M. Ramasse, L. J. Allen, *Phys. Rev. Lett.* **122**, 16103 (2019).

23. C. Dwyer et al., *Phys. Rev. Lett.* **117**, 1–5 (2016).

24. R. Senga et al., *Nature*. **573**, 247–250 (2019).

25. Q. M. Ramasse et al., *Nano Lett.* **13**, 4989–4995 (2013).

26. P. Giannozzi et al., *J. Phys. Condens. Matter*. **21**, 395502 (2009).

27.   E. W. Montroll, R. B. Potts, *Phys. Rev.* **100**, 525–543 (1955).

28.   R. Brout, W. Visscher, *Phys. Rev. Lett.* **9**, 54–55 (1962).

29.   M. T. Hotz et al., *Microsc. Microanal.* **24**, 1132–1133 (2018).

30.   T. Susi et al., *2D Mater.* **4**, 042004 (2017).

31.   Graphenea, (available at https://www.graphenea.com/).

32.   U. Bangert et al., *Nano Lett.* **13**, 4902–4907 (2013).

33.   M. Watanabe, M. Kanno, D. Ackland, C. Kiely, D. Williams, *Microsc. Microanal.* **13**, 1264–1265 (2007).

34.   HREM Research, (available at https://www.hremresearch.com).

35.   F. de la Peña et al., doi:10.5281/zenodo.3396791 (2019).

36.   S. Baroni, S. de Gironcoli, A. Dal Corso, P. Giannozzi, *Rev. Mod. Phys.* **73**, 515–562 (2001).

37.   M. Schlipf, F. Gygi, *Comput. Phys. Commun.* **196**, 36–44 (2015).

38.   J. P. Perdew, K. Burke, M. Ernzerhof, *Phys. Rev. Lett.* **77**, 3865–3868 (1996).

39.   C. Bungaro, S. de Gironcoli, S. Baroni, *Phys. Rev. Lett.* **77**, 2491–2494 (1996).

40.   M. Lazzeri, P. Thibaudeau, *Phys. Rev. B.* **74**, 140301 (2006).

41.   T. Susi et al., *Phys. Rev. Lett.* **113**, 115501 (2014).

42.   F. Wegner, *Zeitschrift für Phys. B Condens. Matter*. **36**, 209–214 (1980).

43.   C. Z. Wang, K. M. Ho, *Phys. Rev. Lett.* **71**, 1184–1187 (1993).
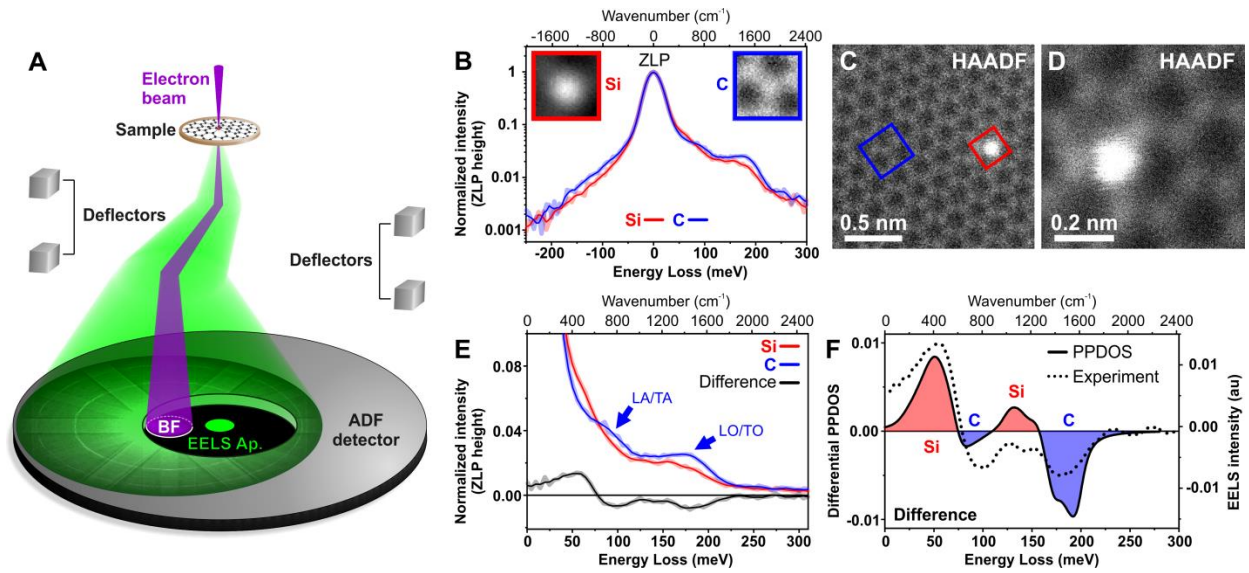
Acknowledgements

Supplementary Materials

Materials and Methods

Supplementary Text

Figures S1-S12

References (*31-43*)

Fig. 1. Experimental geometry and vibrational STEM-EEL spectrum of a Si impurity in graphene. (A) Beam deflectors shift the bright-field (BF) disc away from the EEL spectrometer entrance aperture in the diffraction plane. **(B)** Normalized vibrational EEL spectra of a substitutional Si impurity and of defect-free graphene. Insets show aADF images of the repeatedly scanned sample regions. Smoothed spectra (thin lines) are superimposed on the raw data (transparent thick lines). **(C)** HAADF overview of the experimental region. A red (blue) box indicates the position of the sub-scan region from which the Si (C) spectrum was acquired. **(D)** HAADF close-up of the (bright) trivalent Si impurity. **(E)** Detail of the normalized Si and C EEL spectra shown in B and the difference spectrum. **(F)** Comparison of the calculated differential PPDOS (broadened to match the experimental resolution) and experimental difference spectrum. The blue and red shaded areas highlight energy ranges where the contributions of the Si impurity and its three nearest neighbors, or of bulk graphene, are comparatively stronger.
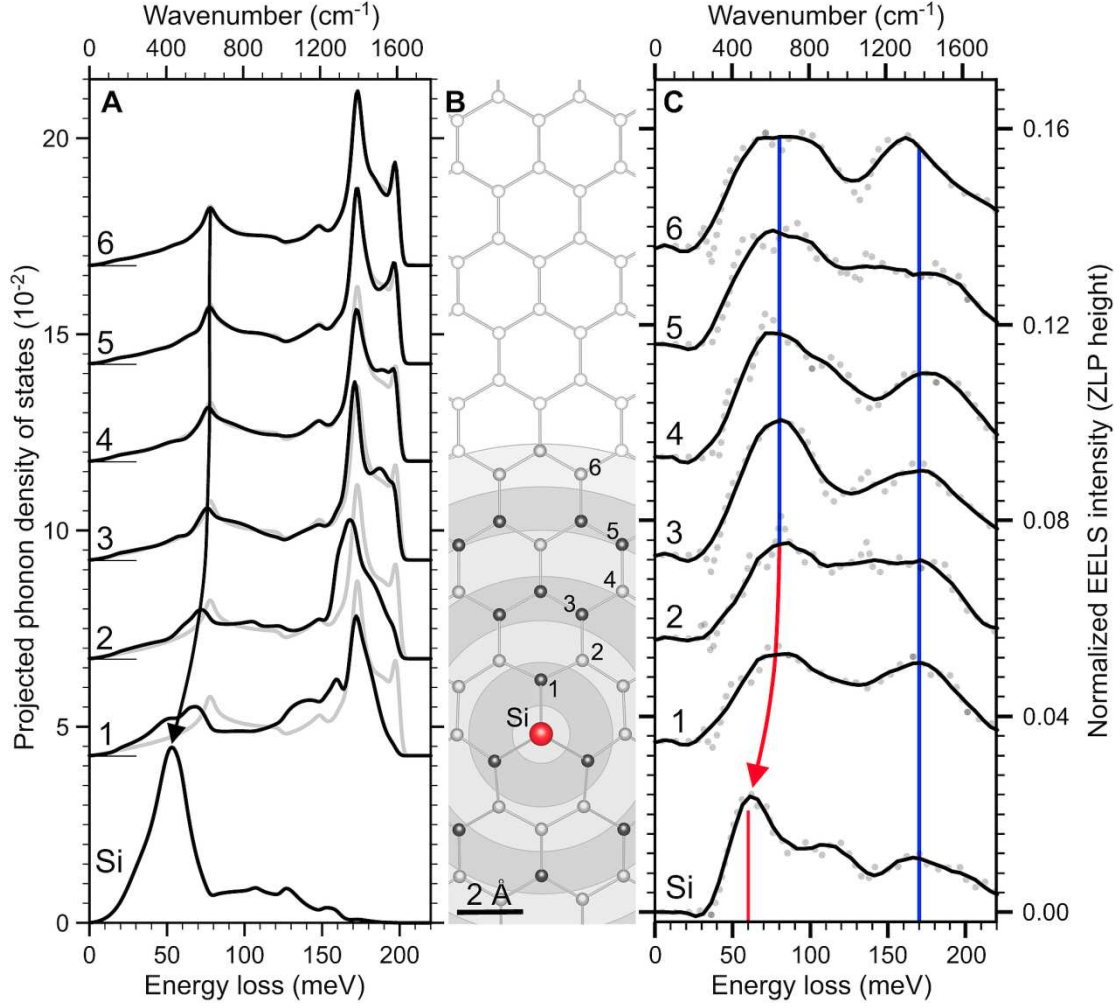
Fig. 2. Localization of the vibrational signal. (A) Black lines: calculated in-plane component of the phonon density of states projected on the Si and carbon atoms at increasing distances from the impurity. Gray lines: bulk graphene phonon density of states per atom, fully recovered from atom 6. The curves are vertically shifted and smeared by a 2 meV FWHM Lorentzian for clarity. **(B)** Sketch of the position of the carbon atoms, labeled 1-6, and Si impurity (red). **(C)** Background-subtracted experimental spectra acquired at equivalent atomic positions. Smoothed (black lines) and raw (gray dots) data are overlaid.
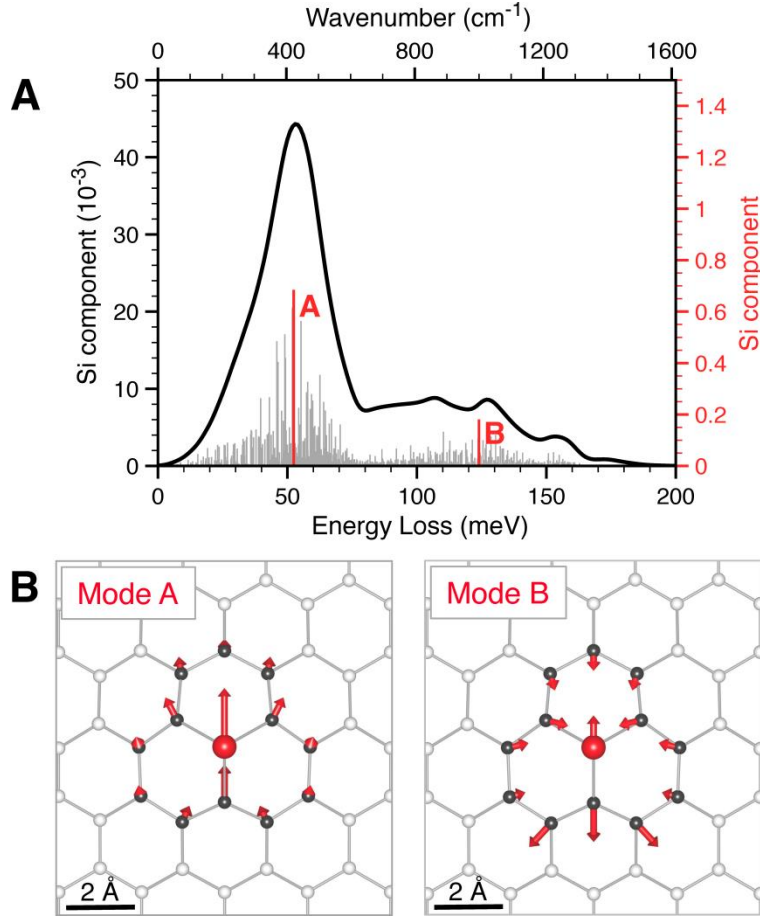
Fig. 3. Localized components of the Si vibrations. **(A)** Gray bar-histogram: square of the phonon eigenmodes of the 96×96 supercell projected on the in-plane Si atom component. Black line: in-plane component of the phonon DOS projected on the Si atom (same as the "Si" PPDOS in fig. 2) obtained by broadening the gray bar-histogram with a 2.0 meV FWHM Lorentzian. The red bar-histogram is calculated from a 13-atom fragment centered on the impurity. Two dominant modes, denoted A and B, are observed. **(B)** Atomic model of the 13-atom fragment (the Si atom is in red), with relative atomic displacements for modes A and B indicated as arrows whose length is proportional to the displacement amplitude.